Supplementary Materials for

Iso-Propagation Vortices with OAM-independent Size and Divergence Towards Future Faster Optical Communications

Wenxiang Yan,[1,2] Zhaozhong Chen,[4] Xian Long, [1,2] Yuan Gao,[1,2] Zheng Yuan,[1,2] Zhi-Cheng Ren,[1,2] Xi-Lin Wang,[1,2] Jianping Ding,[1,2,3,*] and Hui-Tian Wang[1,2,*]

[1]National Laboratory of Solid State Microstructures and School of Physics, Nanjing University, Nanjing 210093, China

[2]Collaborative Innovation Center of Advanced Microstructures, Nanjing University, Nanjing 210093, China

[3]Collaborative Innovation Center of Solid-State Lighting and Energy-Saving Electronics, Nanjing University, Nanjing 210093, China

[4]James Watt School of Engineering, University of Glasgow, Glasgow, G12 8QQ, UK

*Corresponding author: jpding@nju.edu.cn; htwang@nju.edu.cn

Supplementary text:

1. Derivation of equation (4): the innermost ring radius of LGB;
2. Simulation and experimental details for propagation against atmospheric turbulence.
3. Preliminary experiments and orthogonality for IPV multiplexing;
4. Estimated Q_{IPV} value for different S value.
5. Experimental setup for generating the beams in Fig. 2 and observing the self-healing results in Fig. 3.
6. A comparison table among different vortex beams

Supplementary Movies: Movies S1-S7.

Supplementary Reference.

Supplementary text

1. Derivation of equation (3): the innermost ring radius of the LG beam

The amplitude distribution of the LG beam can be written as

$$A_{l,p}(r,\varphi,z)=\left[\frac{w_0}{w(z)}\right]\left[\frac{r}{w(z)}\right]^l \exp(-\frac{r^2}{w^2(z)})L_p^l\left[\frac{2r^2}{w^2(z)}\right]. \tag{S1}$$

Using the approximate relations in refs.[18,41], the right side of Eq. (S1) becomes

$$\left[\frac{r}{w(z)}\right]^l \exp(-\frac{r^2}{w^2(z)})L_p^l\left[\frac{2r^2}{w^2(z)}\right]\approx\frac{\Gamma(p+m+1)}{p!(2N)^{l/2}}J_l(2\sqrt{2N}\frac{r}{w(z)}), p\geq 5, N=p+\frac{l+1}{2}. \tag{S2}$$

The radius of LG beams' innermost ring where the maximum amplitude is located can be derived by searching for the following minimum non-zero solution of $\partial A_{lp}(r,\varphi,z)/\partial r = 0$. Accordingly, it follows that

$$\frac{dJ_l(2\sqrt{2N}\frac{r}{w(z)})}{dr}=0. \tag{S3}$$

Letting $x=2\sqrt{2N}r/w(z)$ and according to equation (5.2.6) in ref.[42] for the Bessel function, $d(J_l(x))/dx=0$ can be rewritten as

$$\frac{dJ_l(x)}{dx}=\frac{1}{2}(J_{l-1}(x)-J_{l+1}(x))=0,\quad x>0, l>0. \tag{S4}$$

Although Bessel functions are infinitely extended functions with an infinite number of extreme points, we will focus our attention on the minimum non-zero extreme point, which is located close to the origin. Using the asymptotic formula (5.2.6) in ref. [42],

$$J_l(x)\approx\frac{x^l}{2^l l!}, \tag{S5}$$

for a small x that meets our requirement, we obtain the following relation

$$\frac{x^{l-1}}{2^{l-1}(l-1)!}-\frac{x^{l+1}}{2^{l+1}(l+1)!}=0, \tag{S6}$$

and the minimum non-zero extreme point of the lth-order Bessel function expressed by

$$x_l\approx 2\sqrt{l(l+1)}. \tag{S7}$$

Owing to the approximation made in Eqs. (S2) through (S5), the actual position of the minimum non-zero extreme point may differ from that determined by Eq. (S7). After scrutinizing the approximating function in Eq. (S7) and the extremum of the Bessel function, the more precise location of the minimum non-zero extreme point is

$$x_l\approx\sqrt{|l|(|l|+1)}+0.77 \quad \text{for } |l|\leq 40; \tag{S8-1}$$

$$x_l\approx|l|+2 \qquad \text{for } |l|>40. \tag{S8-2}$$

For brevity, we only use Eq.(S8-2) in this work. When $m > 4$, the error of Eq. (S8) turns out to be less than 1%. For $m \geq 20$, the error is consistently less than 0.5% and remains below 0.1% for larger values of m. Accounting for $x=2\sqrt{2N}r/w(z)$, we obtain the innermost radius of the LG beam at z as below

$$\rho_l(z)\approx w(z)\frac{0.5|l|+1}{\sqrt{2p+|l|+1}}, \tag{S10}$$

and Eq. (S11) follows immediately at the beam waist plane ($z = 0$),

$$\rho_l(0) \approx w_0 \frac{0.5|l|+1}{\sqrt{2p+|l|+1}}, \tag{S11}$$

The percent error of Eq. (S11) is shown in Fig. S1. When p<5, the error appears to be large and negative (blue area in Fig. S1), which is ascribed to the approximation in Eq. (S2). When l<4, the error is large and positive (red area in Fig. S1), due to the approximation in Eq. (S5). Noticeably when $p \geq 5$ and $l \geq 4$, the error remains to be below 5% and becomes even smaller and insignificant as p and m increase. For the width of the innermost ring, this error is negligible in most cases. Noteworthily, this error does not change with the propagation position z and the beam waist w_0. Hence the error map of Eq. (S10) is the same as that of Eq. (S11), as shown in Fig. S1.

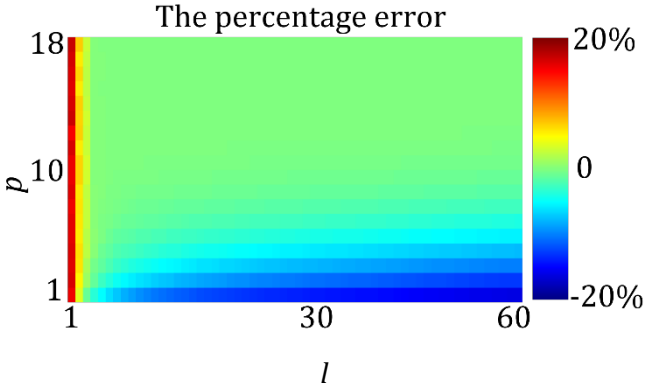

Fig. S1. The percent error of Eq. (S11) varies with *l* and *p*. The percentage error is defined as the ratio between the difference of two innermost radii, respectively calculated from Eq. (S11) and exact LG beams expression, and the exact LGB's innermost radius.

2. Simulation and experimental details for propagation against atmospheric turbulence

To explore the performance of different beams impacted by atmospheric turbulence, we utilized the Modified von Karman turbulence model[43] in our simulation. We assumed a moderate turbulence level, characterized by an optical turbulence strength of $C^2_n = 5\times10^{-15}$ with a propagation distance mesh of Δz = 40 m, a simulation area size of 0.5 m×0.5 m, and turbulence outer and inner scales of 300 m and 0.01 m, respectively. The simulated results averaged 40 trials, such as in Figs. 5(a-d). The procedure and setup for experimental validation are consistent with ref. [27] and are realized by imprinting both the turbulence transmission function and conjugated demultiplexing modes in the SLM2 in Fig. S2(a).

3. Preliminary experiments and orthogonality for IPV multiplexing

Preliminary experiments. The time-varying information carriers in the IPV multiplexing can be expressed as $\sum_{-l_{\max}}^{l_{\max}} A_l(t)e^{i\phi_l(t)}\,\mathrm{LG}_{l,p(l)}(r,\varphi,z)$, wherein l_{max} denotes the highest OAM value, $A_l(t)$ and $\phi_l(t)$ denoting the modulated time-varying amplitude and phase. To further increase the data communication capacity, we can modulate the time-varying amplitude $A_l(t)$ and phase $\phi_l(t)$ using the existing techniques such as quadrature phase-shift keying, amplitude-shift keying, and quadrature amplitude modulation. Besides the existing modulation techniques, the IPV multiplexing is also compatible with wavelength-division multiplexing and polarization-division multiplexing, resulting in a significant improvement of aggregate capacity limit (e. g., Q×2×T×100Gbit/s) of this canonical FSO link system investigated to date. Here we choose to use the binary amplitude-shift keying modulation technology to encode the information into different amplitude sequences of "0"s and "1"s.

Figure S2(a) shows the proof-of-principle experimental scheme under laboratory conditions, where there are four key devices including a laser, two SLMs (Holoeye Leto, 6.6 μm pixel pitch, 1920 ×1080), and a camera. The

SLM1 transmits the multiplexed beams based on the information carrier of $\sum_{-l_{\max}}^{l_{\max}} A_l(t)e^{i\phi_l(t)}\mathrm{LG}_{l,p(l)}(r,\varphi,z)$ at the waist plane z=0. The multiplexed beams propagate in free space for a link distance of z_1 at a meter scale and are partially received by the SLM2 due to their limited size; the recordable beam size depends on the mode order and link distance due to diffraction-induced expansion. For demultiplexing, the SLM2 is imprinted with a Dammann grating pattern produced from the conjugated LG modes and truncated by a circular mask, $\sum_{-l_{\max}}^{l_{\max}} \mathrm{LG}^{*}_{l,p(l)}(r,\varphi,z_1)\exp(i2\pi u_l x + i2\pi v_l y)\mathrm{circ}(r/R_0)$. The circular mask with a radius of $2.5w_1(z_1) \approx 3$ mm acting as the receiver aperture (Fig. S2(c)) constitutes an FSO link system with S = 6.25 (ref. [40]). The SLM2 diffracts each multiplexed subchannel into a different direction and then is then focused by a lens on the distinct area of a camera (PCO. edge 4.2 bi, 6.5 μm pixel pitch, 2048 ×2048), accomplishing the IPV demultiplexing by the Dammann grating. We use the integral intensity over all the pixels of the accumulated region (yellow-dotted circle in Fig. S2(f)) in the central area of each demultiplexing subchannel to identify whether the bit values are 1 or 0 based on a predetermined discrimination threshold.

When M^2_{IPV} = 0.9S = 5.6, all IPVs with mode l and M^2_{IPV} = 5.6 are compatible with the FSO system. This implies a more substantial subchannel array. It's imperative to recognize that existing spatial light modulators, commercially available, present constraints related to panel and pixel dimensions, impacting the precise projection of structured beams with elevated mode orders. For example, the IPV with l = 92 where the phase changes 92 cycles azimuthally may not be able to be accurately projected on the SLM1 (Holoeye Leto, 6.6 μm pixel pitch, 1920 ×1080). For safety, we preliminarily tested the IPV multiplexing incorporating 105 IPV subchannels with l = [-52, 52]. More feasible subchannels and larger capacity IPV multiplexing communication can be further boosted by the adoption of metasurface platforms with large panel sizes and ultra-high resolution. Considering the panel of the carema, we tested the independent addressability of subchannels in two segments: an 8-bit binary amplitude-shift keying en/decoding IPV multiplexing for $|l|\in[38, 52]$ that assigned bits 1-8 to $(l, p(l))$ = (52, 50), (-50, 45), (48, 41), (-46, 37), (44, 33), (-42, 29), (40, 26), (-38, 22), respectively, and a 16-bit binary amplitude-shift keying en/decoding IPV multiplexing for $|l|\in[2, 30]$ that assigned bits 1-16 to $(l, p(l))$ = (32, 14), (-30, 11), (28, 9), (-26, 7), (24, 5), (-22, 3), (20, 2), (-18, 1), (16, 0), (-14, 0), (12, 0), (-10, 0), (8, 0), (-6, 0), (4, 0), (-2, 0), respectively. The experimental results of 256 cases of the 8-bit IPV multiplexing are shown in Figs. S2(g-i), exhibiting a bit error rate (BER) of zero via a discrimination threshold in [0.2, 0.4]. The decoding results of the 16-bit IPV multiplexing are shown in Figs. S2(j-m).

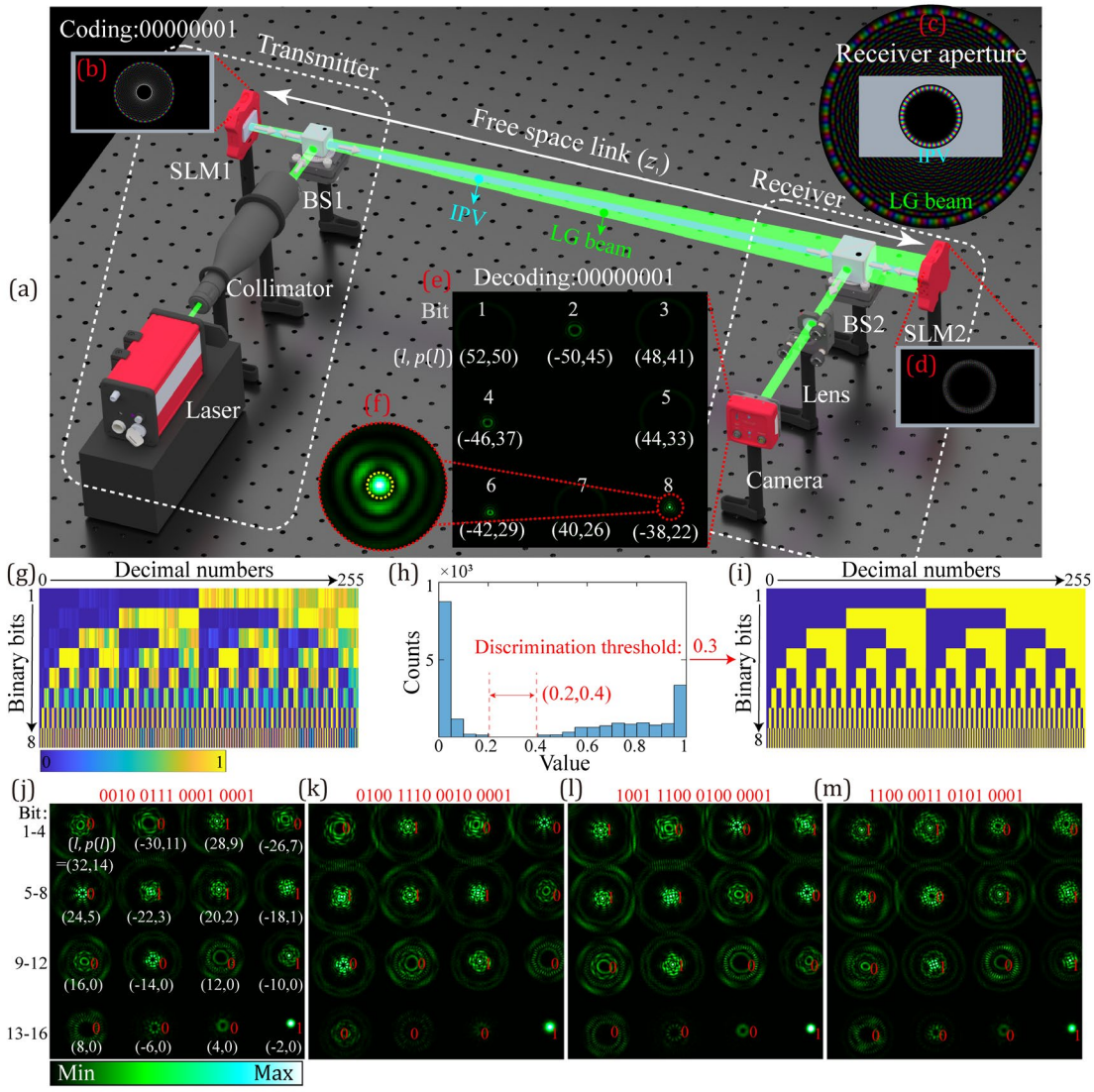

Fig. S2. Preliminary demonstration of IPV multiplexing (lenses omitted). (a) Experimental setup: BS1-2, beam splitters; SLM1-2, reflective phase-only spatial light modulators. The insets: (b), the complex distribution of $LG_{-38,22}(r, \varphi, 0)$ imprinted on the SLM1; (c), the complex distribution of $LG_{-38,22}(r, \varphi, z_1)$ truncated by the receiver aperture $\mathrm{circ}(r/R_0)$ of the SLM2; (d), the complex distribution of truncated Dammann grating $\sum_{-l_{\max}}^{l_{\max}} \mathrm{LG}^{*}_{l,p(l)}(r,\varphi,z_1)\exp(i2\pi u_l x + i2\pi v_l y)\mathrm{circ}(r/R_0)$ imprinted on the SLM2. (e), the demultiplexing intensity pattern on the camera. (f), the zoomed-in view of bit 8 on (e) with a yellow-dotted circle depicting the accumulated region of the central area. (g) Accumulated values (a.u.) of the accumulated region of 256 cases in the 8-bit IPV multiplexing shown in (e). (h) Corresponding distribution histograms of (g). (i) Binarized results of (g) with discrimination threshold 0.3. Supplementary Movie S6 (MP4, 1.14MB) shows the experimental demultiplexing intensity patterns of the 256 cases of (g-i). (j-m) Experimental decoded intensity patterns of 16-bit IPV multiplexing within $|l| \in [2, 32]$ of decimal numbers 10001, 20001, 40001, and 50001, respectively; the white and red font digits indicate the modes and the bit values.

Orthogonality and transmission matrix of IPV multiplexing. The orthonormality of the normalized LG beam, as shown in Fig. S3(a), can be expressed as

$$\begin{aligned}\left\langle \mathrm{LG}_{l_1,p_1} \middle| \mathrm{LG}_{l_2,p_2} \right\rangle &= \iint_{\infty} \mathrm{LG}_{l_1,p_1}(r,\varphi,z_1) \times \mathrm{LG}^{*}_{l_2,p_2}(r,\varphi,z_1) r dr d\varphi \\ &= \int_0^{\infty} \mathrm{LG}_{l_1,p_1}(r,z_1) \times \mathrm{LG}^{*}_{l_2,p_2}(r,z_1) r dr \int_0^{2\pi} e^{il_1\varphi} e^{-il_2\varphi} d\varphi = \delta_{(l_1,l_2),(p_1,p_2)},\end{aligned} \tag{S12}$$

where $\mathrm{LG}_{l,p}(r,\varphi,z_1) = \mathrm{LG}_{l,p}(r,z_1)e^{il\varphi}$. When the circular receiver aperture circ(r/R_0) truncates the LG beam to get the innermost-ring-based IPV with modes (l, p(l)) at $z = z_1$, with circ(·) denoting the circular function, Eq. (S12) becomes

$$\begin{aligned}&\left\langle \mathrm{LG}_{l_1,p(l_1)} \mathrm{circ}(r/R_0) \middle| \mathrm{LG}_{l_2,p(l_2)} \mathrm{circ}(r/R_0) \right\rangle \\ &= \iint_{\infty} \mathrm{LG}_{l_1,p(l_1)}(r,\varphi,z_1) \times \mathrm{LG}^{*}_{l_2,p(l_2)}(r,\varphi,z_1) \mathrm{circ}(r/R_0) r dr d\varphi \\ &= \int_0^{R_0} \mathrm{LG}_{l_1,p(l_1)}(r,z_1) \times \mathrm{LG}^{*}_{l_2,p(l_2)}(r,z_1) r dr \int_0^{2\pi} e^{il_1\varphi} e^{-il_2\varphi} d\varphi \\ &= \left(\int_0^{\infty} \mathrm{LG}_{l_1,p(l_1)_1}(r,z_1) \times \mathrm{LG}^{*}_{l_2,p(l_2)}(r,z_1) r dr - \int_{R_0}^{\infty} \mathrm{LG}_{l_1,p_1}(r,z_1) \times \mathrm{LG}^{*}_{l_2,p(l_2)}(r,z_1) r dr \right) \int_0^{2\pi} e^{il_1\varphi} e^{-il_2\varphi} d\varphi \\ &= \delta_{(l_1,l_2),(p(l_1),p(l_2))} - 2\pi\delta_{(l_1,l_2)} \int_{R_0}^{\infty} \mathrm{LG}_{l_1,p(l_1)}(r,z_1) \times \mathrm{LG}^{*}_{l_2,p(l_2)}(r,z_1) r dr\end{aligned} \tag{S13}$$

If $l_1 \neq l_2$, Eq. (S13) equals 0, thus verifying the orthogonality of distinct azimuthal modes (i.e. OAM orthogonality). When $l_1 = l_2 = l$ but $p_1 \neq p_2$, Eq. (S12)can be expressed as

$$\left\langle \mathrm{LG}_{l,p_1} \mathrm{circ}(r/R_0) \middle| \mathrm{LG}_{l,p_2} \mathrm{circ}(r/R_0) \right\rangle = -2\pi \int_{R_0}^{\infty} \mathrm{LG}_{l_1,p_1}(r,z_1) \times \mathrm{LG}^{*}_{l_2,p_2}(r,z_1) r dr, \tag{S14}$$

which is nonzero. Hence, innermost rings with the same OAM but distinct radial modes are no longer orthogonal, as shown in Fig. S3(c). The orthogonality of the IPVs, as shown in Fig. S3(b), can be expressed as

$$\left\langle \mathrm{LG}_{l_1,p(l_1)}(r,\varphi,z_1) \mathrm{circ}(r/R_0) \middle| \mathrm{LG}_{l_2,p(l_2)}(r,\varphi,z_1) \mathrm{circ}(r/R_0) \right\rangle = \begin{cases} 0 & l_1 \neq l_2 \\ \eta(l) & l_1 = l_2 = l \end{cases}, \tag{S15}$$

where the efficiency $\eta(l)$, which is the ratio of power falling in the aperture (i.e., the power of the innermost ring) to the entire beam, is represented by $\left\langle \mathrm{LG}_{l,p(l)}(r,\varphi,z_1) \mathrm{circ}(r/R_0) \middle| \mathrm{LG}_{l,p(l)}(r,\varphi,z_1) \mathrm{circ}(r/R_0) \right\rangle$.

For demultiplexing with uniform OAM spectrum, the SLM2 is imprinted with a Dammann grating pattern produced from the conjugated LG modes with energy normalization coefficient $\eta^{-1}(l)$, i.e., $\sum \eta^{-1}(l) \mathrm{LG}^{*}_{l,p(l)}(r,\varphi,z_1) \exp(i2\pi u_l x + i2\pi v_l y) \mathrm{circ}(r/R_0)$. Thus we accomplished the IPV demultiplexing with the uniform power spectrum of OAM for the IPVs, as follows

$$\left\langle \mathrm{LG}_{l_1,p(l_1)}(r,\varphi,z_1) \mathrm{circ}(r/R_0) \middle| \eta^{-1}(l_2,p(l_2)) \mathrm{LG}_{l_2,p(l_2)}(r,\varphi,z_1) \mathrm{circ}(r/R_0) \right\rangle = \delta_{l_1,l_2}. \tag{S16}$$

The orthonormality of Eq. (S16) is illustrated in Fig. S3(d).

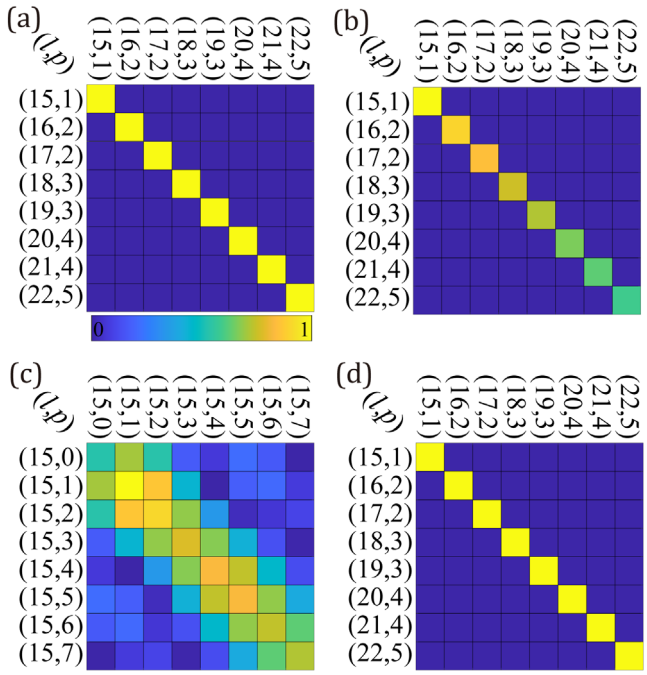

Fig. S3. Orthogonality of truncated LG beams with *m*. (a) Confusion matrix of normalized LG beams with modes identical to Fig. 6(e). (b) Confusion matrix of truncated LG beams with distinct *l*, which are truncated by the receiver aperture (the yellow-dotted circles) in Fig. 6(e). (c) Confusion matrix of truncated LG beams with the same *l*=15 and distinct *p*. (d) Confusion matrix of the IPV demultiplexing in Eq. (S16).

Let the transmitted and received signals at time t be $\boldsymbol{s}(t)=\left[s_1(t) \quad s_2(t) \quad \cdots \quad s_M(t)\right]$ and $\boldsymbol{r}(t)=\left[r_1(t) \quad r_2(t) \quad \cdots \quad r_M(t)\right]$. As the FSO system is linear, the input and output are related by a transmission matrix $\boldsymbol{h}$ so that $\boldsymbol{r}(t)=\boldsymbol{h}\bullet\boldsymbol{s}(t)$. Under the assumption of perfect demultiplexing, the transmission matrix of IPV multiplexing is diagonal with the matrix elements[6] represented by $h_{l,n}=\sqrt{\eta(l)}\delta_{l,n}$. Since the off-diagonal elements of $\boldsymbol{h}$ are zeros, the IPV multiplexing promises minimal channel crosstalk in communication experiments.

4. **Estimated Q_{IPV} with different S.**

IPV multiplexing maximizes the receiving efficiency. Figure S4(a) presents the schematic of FSO communication using data-carrying IPVs, excluding lenses. Due to diffraction-induced mode-dependent expansion, a finite-size receiver results in significant power loss in the mode-division multiplexing, such as OAM multiplexing and LG (HG) beam multiplexing. Specifically, for l > 5, LG beams or OAM modes are obstructed by the receiver aperture with parameters R_0 = 2.5$w(z_1)$ and S =6.25. As l approaches 15, those beams lose nearly all power, as indicated by the red curves in Figs. S4(b) and (c). Nonetheless, our approach of extracting data from these innermost-ring-based IPVs with global M^2_{IPV} =0.9S <S, which always passes through the receiver aperture with selected radial index $p(l)$ (as illustrated by the blue curve in Fig. S4(b)), results in enhanced total received power (as shown by the blue curve and orange shadow area in Fig. S4(c)).

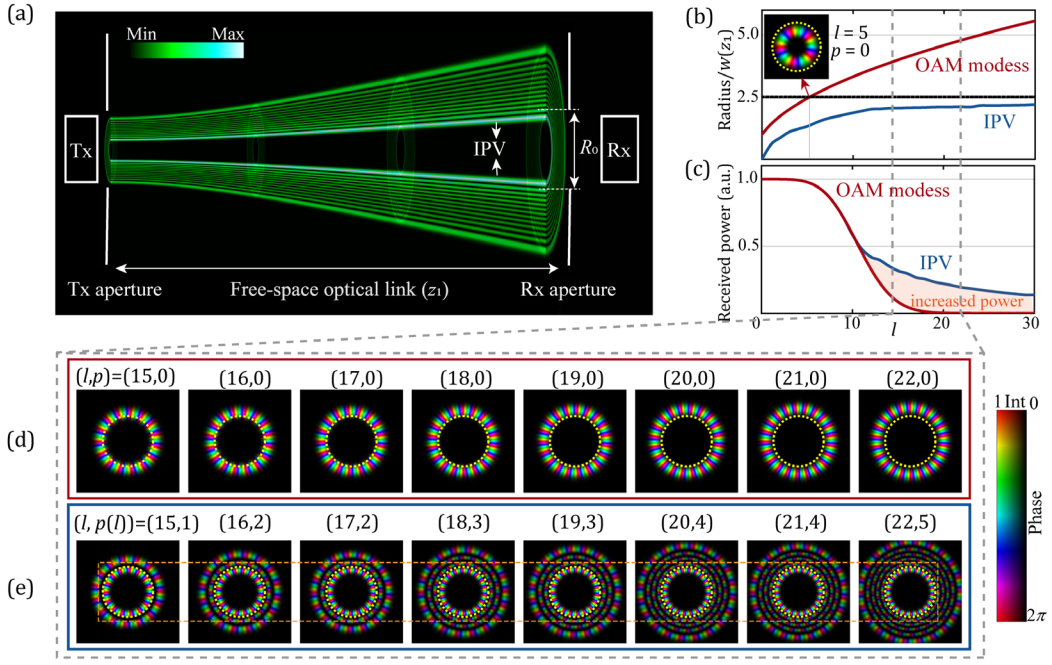

Fig. S4. Schematic view of FSO communication using data-carrying IPVs (lenses omitted). (a) A limited-size receiver of radius $R_0 = 2.5w$ (z_1) at a link distance z_1 obstructs the LG beam due to large size and rapid divergence, but allows the innermost-ring-based IPV to pass through. (b) Dependence of the required receiver aperture radius on the azimuthal index l: the red curve, $\rho_{OAM}(z_1)$ of mode (l, 0); the blue curve, $\rho_{IPV}(z_1)$ of mode (l, $p(l)$); the black-dashed line, $R_0 = 2.5w(z_1)$ of the limited-size aperture. The inset in (b) shows the complex distribution of $LG_{5,0}(r, \varphi, z_1)$ and the yellow-dotted circle represents the receiver aperture. (c) Received power of $LG_{l,0}(r, \varphi, z_1)$ (red curve) and $LG_{l, p(l)}(r, \varphi, z_1)$ (blue curve), with the orange shadow area indicating the increasing power between the two curves. Complex distributions of (d) OAM modes and (e) IPVs with l ranging from 15 to 22, where the yellow-dotted circle represents the receiver aperture as well.

Unlike the conventional OAM multiplexing which uses only the azimuthal degree of freedom (φ), the LG beam multiplexing exploits both two spatial degrees of freedom (r, φ) of the system and thus makes better use of always limited spatial resources, thanks to the orthogonality of modes with l and p. In practical FSO systems, the limited-size receiver aperture truncates the r dimension, which leads to radial index p non-orthogonal, while only azimuthal index l remains orthogonal. Namely, only the orthogonality of OAM holds, as detailed in Supplementary Note 3. Accordingly, Q is determined by the number of l solutions for $M^2_{IR}(l, p) < S$. *To maximize the received power for each subchannel of the limited-size receiver, the radial index p should be optimized for a given l, i.e.,* $p_{opt}(l)$. For low-order OAM modes with their beam size smaller than the receiver aperture (i.e. $M^2_{LG}(l, p=0) \leq S$), we can select $p_{opt}(l) = 0$. For higher-order modes with larger beam sizes, we can increase p to a critical value to decrease r_{IR} in Eq. (3) such that the innermost ring of the beam can just fall within the receiver aperture, and **coincidentally, it reaches the maximum efficiency right now, as illustrated in Fig. S5.** This critical value is $p = p_{opt}(l)$**.** The innermost rings with mode (l, $p_{opt}(l)$), received by the receiver aperture, have the approximative identical global quality factor M^2_{IR} (or namely, aforementioned M^2_{IPV}) and thus have OAM-independent size and divergence during propagation, i.e., aforementioned IPVs. Therefore, $p_{opt}(l) \approx p(l) = \text{round}((0.5|l|+1)^2/2M^2_{IPV}-0.5(|l|+1))$, as displayed in Fig. S5(b). For low-order OAM modes with $M^2_{LG}(l, 0) < M^2_{IPV}$, the calculated $p(l)$ will be negative and thus set to 0 for optimized received power. **Hence, the IPV multiplexing strategy maximizes the receiving efficiency and minimizes power loss.**

Figure S5(a) shows the receiving efficiency, $\eta(l,p)$, as the ratio of the power in the receiver aperture to that of the entire beam, in an FSO link system with a given S = 6.25. The dashed line in Fig. S5(a) represents the highest efficiency $\eta_{max}(l)$ for a given l and the corresponding optimized $p_{opt}(l)$. $p_{opt}(l)$ is highly consistent with $p(l)$ with M^2_{IPV}=0.9S, as displayed in Fig. S5(b) and thus, we will no longer distinguish between $p_{opt}(l)$ and $p(l)$. In Fig. S5(c), we compared the receiving ability of LG beam multiplexing, OAM multiplexing, and IPV multiplexing (M^2_{IPV}=0.9S) in an FSO link system with S = 6.25, using the curves of $M^2_{LG}(l, p(l))$, $M^2_{OAM}(l)$, and M^2_{IPV}, and found that only M^2_{IPV} is always less than S, indicating that the innermost-ring-based IPVs with subchannels $(l, p(l))$ can always pass through the receiver aperture. Hence, only the IPV multiplexing can be always accomplished by this practical FSO link system with optimized received efficiency, while LG beam multiplexing and OAM multiplexing are highly confined by the system ($M^2_{LG} > M^2_{OAM} > S$ = 6.25 when $l > 5$).

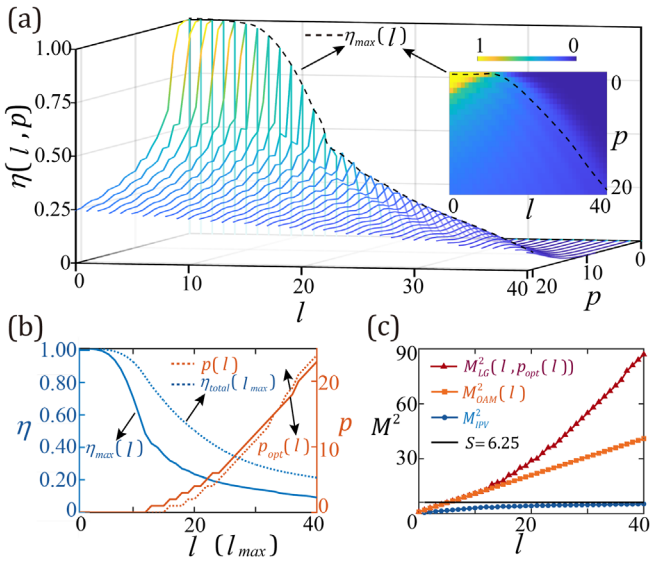

Fig. S5. Reception efficiency of LG beam. (a) Receiving efficiency $\eta(l,p)$ for l in [0,40] and p in [0, 23]; the dashed lines represent the highest efficiency $\eta_{max}(l)$ versus (l,p). (b) Curves of $\eta_{max}(l)$ (blue), the total receiving efficiency $\eta_{\text{total}}(l_{\text{max}}) = \sum_{-l_{max}}^{l_{max}} \eta(l) / (2l_{\text{max}}+1)$ (blue-dotted), $p_{opt}(l)$ (orange), and $p(l)$ (orange-dotted). (c) $M^2_{LG}(l, p_{opt}(l))$, $M^2_{OAM}(l)$, and M^2_{IPV} (represented by red-triangle, orange-square, and blue-circle curves, respectively) versus the transmission capability of the FSO link system with S = 6.25 (black line).

Estimated Q_{IPV} value for different S value. For a more comprehensive comparison for subchannels of different spatial multiplexing techniques, we estimated Q_{IPV} value for different S as $Q_{IPV} \approx 2\text{floor}[C(\eta_{total})S]+1$, which attains a approximate $C(\eta_{total})$-fold improvement for most systems compared with traditional OAM multiplexing of $Q_{OAM} \approx 2\text{floor}[S]+1$. $C(\eta_{total})$ is empirical constant-coefficient and sharply increases as the total reception efficiency η_{total} decreases, as displayed in Fig. S6(a) and Table S1. The total reception efficiency η_{total} is associated with the sidelobe energy inefficiency in optical communication, as illustrated in Fig. S4, while the innermost-ring-based IPVs primarily govern the interaction with external sensors or matter.

As a result, when the laser power and detector sensitivity are abundant, the number of independent subchannels for IPV multiplexing can be remarkably enhanced (i.e., increasing Q_{IPV} ($\approx 2\ \text{floor}[C(\eta_{total})S^2]+1$)) at the cost of sidelobe energy inefficiency (i.e., decreasing η_{total}). On the other hand, for conventional spatial multiplexing techniques such as OAM multiplexing, LG (HG) beam multiplexing, and MIMO transmission, increasing the laser

power or detector sensitivity only enhances the signal-to-noise ratio (SNR) but cannot enhance the number of independent subchannels. **Therefore, the IPV multiplexing offers a unique trade-off between the SNR and *Q*, potentially advancing future faster optical communications with more modes.**

As an example, in the preliminary experiments, the laser (Coherent Verdi G5: 5W max power) and the camera (PCO. edge 4.2 bi: 16-bit gray value, 95% QE, 0.2 e-/pixel/s dark current, air and water cooled with the lowest temperature -40°C), allows a total reception efficiency of η_{total} = 20% which corresponds to $C(0.2)$=14.76. The empirical subchannel number of IPV multiplexing (Emp. Q_{IPV}, the pink-dashed curve) is given by 2floor[14.76S]+1, which agrees well with the actual results (Q_{IPV}, the blue curve) in Fig. S6(b). As illustrated in Fig. 6(c), Q_{IPV} steadily attains a 14-fold improvement for traditional OAM multiplexing with different S. For practical FSO systems with limited-size receivers and S<30, IPV multiplexing offers more subchannels than spatial multiplexing technique, such as LG beam multiplexing, HG beam multiplexing, and conventional MIMO transmission, as illustrated in Figs. 6(b-c). For instance, in the preliminary experiments with given S = 6.25, the Q_{IPV} = 185, in contrast to Q_{OAM} = 13, Q_{LG} (Q_{HG}) = 21, Q_{MIMO} = 35, respectively.

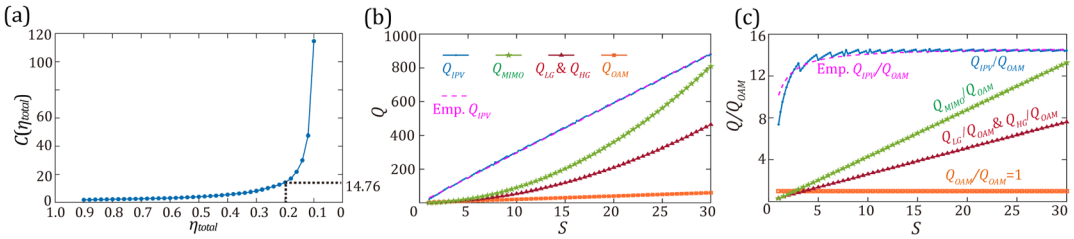

Fig. S6. Numbers of independent spatial subchannels with different *S*. (a) Empirical constant coefficient $C(\eta_{total})$ versus η_{total} (the corresponding look-up table displayed in Table S1); the black-dotted lines depict $C(0.2)$ = 14.76. (b) Numbers Q of independent spatial subchannels for spatial multiplexing techniques from S = 1 to S = 30 with η_{total} = 20% for IPV multiplexing; Emp.: Empirical. (c) The improvement of Numbers of independent spatial subchannels in (b) versus Q_{OAM}.

η_{total}	0.90	0.88	0.86	0.84	0.82	0.80	0.78	0.76	0.74	0.72
$C(\eta_{total})$	2.01	2.08	2.20	2.27	2.34	2.41	2.46	2.54	2.60	2.67
η_{total}	0.70	0.68	0.66	0.64	0.62	0.60	0.58	0.56	0.54	0.52
$C(\eta_{total})$	2.72	2.88	2.93	3.07	3.14	3.27	3.41	3.59	3.80	4.02
η_{total}	0.50	0.48	0.46	0.44	0.42	0.40	0.38	0.36	0.34	0.32
$C(\eta_{total})$	4.20	4.47	4.73	5.01	5.32	5.74	6.13	6.61	7.06	7.67
η_{total}	0.30	0.28	0.26	0.24	0.22	0.20	0.16	0.14	0.12	0.10
$C(\eta_{total})$	8.33	9.32	10.34	11.44	12.78	14.76	21.88	30.01	47.63	114.68

Table S1. Empirical constant coefficient $C(\eta_{total})$ versus η_{total}. The red fonts indicates that $C(0.2)$ = 14.76.

5. Experimental setup for generating the beams in Fig. 2 and observing the self-healing results in Fig. 3.

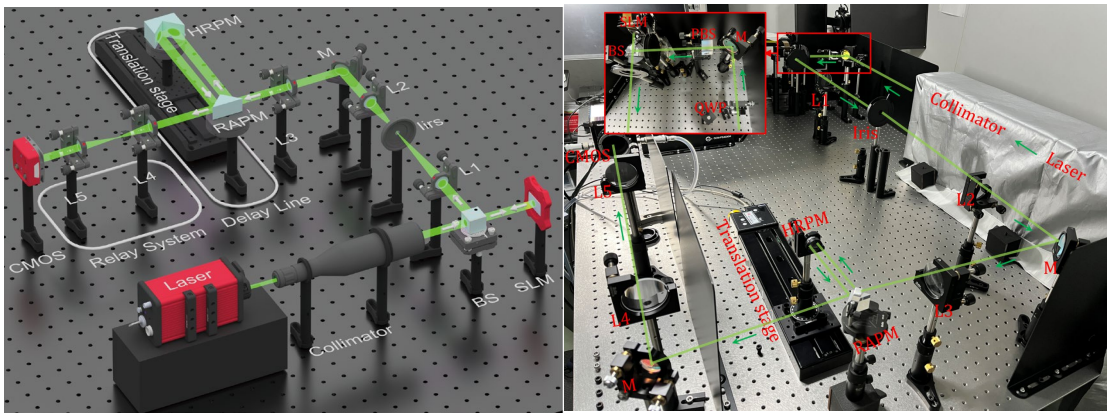

Fig. S7. The schematic (left) and actual (right) experimental apparatus for generating and detecting IPVs. BS, beam splitter; SLM, phase-only spatial light modulator; L1-L5, lens; M, mirror; RAPM, right-angle prism mirror; HRPM, hollow roof prism mirror; CMOS, complementary metal oxide semiconductor camera; PBS, polarizing beam splitter; QWP, quarter-wave plate. The green arrows indicate the direction of the light path.

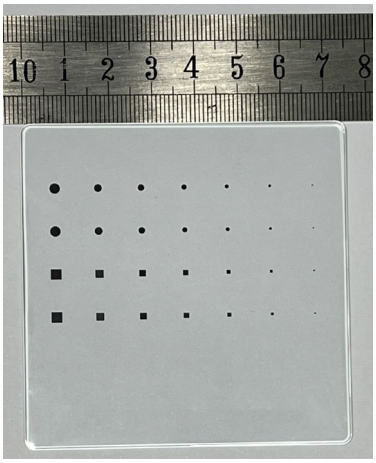

Fig. S8. The obstacle mask with photoetching chrome patterns on a glass substrate, used in Fig. 3.

6. A comparison table among different vortex beams

Feature	Traditional Vortex Beams	Perfect Vortex Beams	Iso-Propagation Vortices
Size	OAM-dependent	OAM-independent near focal plane	**OAM-independent**
Divergence	OAM-dependent	OAM-dependent	**OAM-independent**
Self-Restoration	Limited	Limited	**Enhanced**
Modal Scattering	Higher in turbulence	Reduced near focal plane	**Reduced and uniform**
Practical Application	Limited by beam expansion and divergence	Limited by focal plane constraints	**Suitable for long-distance communication, imaging, and quantum information processing**

Table S2. Comparison among traditional vortex beams, perfect vortex beams, and Iso-Propagation Vortex beams.

Supplementary Movies

Movie S1. Experimental movie for the self-healing process of the IPV with the aid of sidelobes in Fig. 3(e).

Movie S2. Corresponding transversal energy flow density of the self-healing process in Fig. 3(f).

Movie S3. Experimental movie that the OAM modes will not self-heal after being impaired without the "energy reservoir" of the sidelobes, shown in Fig. 3(g).

Movie S4. Corresponding transversal energy flow density shown in Fig. 3(h).

Movie S5. Those 105 subchannels of IPV multiplexing with l = [-52, 52], S = 6.25, and $M^2_{IPV} = 0.9S = 5.6$.

Movie S6. Experimental demultiplexing intensity maps of the 256 cases on the Camera of Figs. S2(g-i).